X-ray Bragg magnifier microscope as a linear shift invariant imaging system: image formation and phase retrieval

P. Vagovič,[1,*] L. Švéda,[2] A. Cecilia,[3] E. Hamann,[3] D. Pelliccia,[4] E. N. Gimenez,[5] D. Korytár,[6] K. M. Pavlov,[4,7] Z. Zápražný,[6] M. Zuber,[3] T. Koenig,[3] M. Olbinado,[8] W. Yashiro,[8] A. Momose,[8] M. Fiederle,[3] and T. Baumbach[3]

[1] *Center for Free-Electron Laser Science, Deutsches Elektronen-SYnchrotron, Hamburg, Germany*
[2] *FNSPE CTU, Prague, Czech Republic*
[3] *ANKA Light Source, Karlsruhe Institute of Technology, Karlsruhe, Germany*
[4] *School of Physics,Monash University, Victoria 3800, Australia*
[5] *Diamond Light Source, England*
[6] *Institute for Electrical Engineering, Slovak Academy of Sciences, Bratislava, Slovakia*
[7] *University of New England, Armidale NSW 2351 Australia*
[8] *Institute of Multidisciplinary Research for Advanced Materials, Tohoku University, Japan*
[*]patrik.vagovic@desy.de

Abstract: We present the theoretical description of the image formation with the in-line germanium Bragg Magnifier Microscope (BMM) and the first successful phase retrieval of X-ray holograms recorded with this imaging system. The conditions under which the BMM acts as a linear shift invariant system are theoretically explained and supported by the experiment. Such an approach simplifies the mathematical treatment of the image formation and reconstruction as complicated propagation of the wavefront onto inclined planes can be avoided. Quantitative phase retrieval is demonstrated using a test sample and a proof of concept phase imaging of a spider leg is also presented.

References

1. P. Vagovič, D. Korytár, A. Cecilia, E. Hamann, L. Švéda, D. Pelliccia, J. Härtwig, Z. Zápražný, P. Oberta, I. Dolbnya, K. Shawney, U. Fleschig, M. Fiederle, and T. Baumbach, "High-resolution high-efficiency X-ray imaging system based on the in-line Bragg magnifier and the Medipix detector," J. Synchrotron Radiat. **20**, 153–159 (2013).
2. W. J. Boetinger, H. E. Burdette, and M. Kuriyama, "X-ray magnifier," Rev. Sci. Instrum. **50**, 26–30 (1979).
3. M. Kuriyama, R. C. Dobbyn, R. D. Spal, H. E. Burdette, and D. Black, "Hard x-ray microscope with submicrometer spatial resolution," J. Res. Natl. Inst. Stand. Technol. **95**, 559 (1990).
4. G. Stampanoni, R. Borchert, R. Abela, and P. Rüegsegger, "Bragg magnifier: A detector for submicrometer X-ray computer tomography," J. Appl. Phys. **92**, 7630–7635 (2002).
5. P. Schäfer and R. Köhler, "Asymmetric Bragg reflection as X-ray magnifier," J. Phys. D: Appl. Phys. **36**, A113–A117 (2003).
6. P. Modregger, D. Lübbert, P. Schäfer, and R. Köhler, "Magnified X-ray phase imaging using asymmetric Bragg reflection: Experiment and theory," Phys. Rev. B. **74**, 054107 1–10 (2006).
7. R. A. Senin, A. V. Buzmakov, A. V. Konovko, I. S. Smirnov, A. S. Geranin, and V. E. Asadchikov, "Gain in spatial resolution of X-ray laboratory microtomographs with enlarging X-ray optical elements," JPCS **186** (2009).

8. K. Hirano, Y. Takahashi, and H. Sugiyama, "Development and application of variable-magnification X-ray Bragg magnifiers," Nucl. Instr. Meth. Phys. Res. A **741**, 78 – 83 (2014).

9. P. Vagovič, D. Korytár, P. Mikulík, A. Cecilia, C. Ferrari, Y. Yang, D. Hänschke, E. Hamann, D. Pelliccia, T. A. Lafford, M. Fiederle, and T. Baumbach, "In-line Bragg magnifier based on V-shaped germanium crystals," J. Synchrotron Radiat. **18**, 753–760 (2011).

10. W. Pauli, *Die allgemeinen Prinzipien der Wellenmechanik* (Handb. Phys., 1933).

11. G. Taylor, "The phase problem," Acta Crystallogr. Sect. D **59**, 1881–1890 (2003).

12. J. R. Fienup, "Phase retrieval algorithms: a comparison," Appl. Opt. **21**, 2758–2769 (1982).

13. J. R. Fienup, "Reconstruction of a complex-valued object from the modulus of its Fourier transform using a support constraint," J. Opt. Soc. Am. A **4**, 118–123 (1987).

14. R. W. Gerchberg and W. O. Saxton, "A practical algorithm for the determination of phase from image and diffraction plane pictures," Optik **35**, 237 (1972).

15. T. E. Gureyev and K. A. Nugent, "Phase retrieval with the transport-of-intensity equation. II. orthogonal series solution for nonuniform illumination," J. Opt. Soc. Am. A **13**, 1670–1682 (1996).

16. A. Burvall, U. Lundström, P. A. C. Takman, D. H. Larsson, and H. M. Hertz, "Phase retrieval in X-ray phase-contrast imaging suitable for tomography," Opt. Express **19**, 10359 (2011).

17. P. Cloetens, W. Ludwig, J. Baruchel, D. Van Dyck, J. Van Landuyt, J. P. Guigay, and M. Schlenker, "Holotomography: Quantitative phase tomography with micrometer resolution using hard synchrotron radiation X-rays," Appl. Phys. Lett. **75**, 2912–2914 (1999).

18. P. Modregger, D. Lübbert, P. Schäfer, R. Köhler, T. Weitkamp, M. Hanke, and T. Baumbach, "Fresnel diffraction in the case of an inclined image plane," Opt. Express **16**, 5141–5149 (2008).

19. D. Paganin, *Coherent X-Ray Optics* (Oxford University, 2006).

20. A. Authier, *Dynamical Theory of X-ray Diffraction* (Oxford University, 2004).

21. K. M. Pavlov, T. E. Gureyev, D. Paganin, Y. I. Nesterets, M. J. Morgan, and R. A. Lewis, "Linear systems with slowly varying transfer functions and their application to x-ray phase-contrast imaging," J. Phys. D: Appl. Phys. **37**, 2746 (2004).

22. K. Pavlov, T. Gureyev, D. Paganin, Y. Nesterets, M. Kitchen, K. Siu, J. Gillam, K. Uesugi, N. Yagi, M. Morgan, and R. Lewis, "Unification of analyser-based and propagation-based X-ray phase-contrast imaging," Nucl. Instr. Meth. Phys. Res. A **548**, 163–168 (2005).

23. P. Coan, E. Pagot, S. Fiedler, P. Cloetens, J. Baruchel, and A. Bravin, "Phase-contrast X-ray imaging combining free space propagation and Bragg diffraction," J. Synchrotron Radiat. **12**, 241–245 (2005).

24. D. Paganin and K. A. Nugent, "Noninterferometric phase imaging with partially coherent light," Phys. Rev. Lett. **80**, 2586–2589 (1998).

25. T. Latychevskaia and H.-W. Fink, "Solution to the twin image problem in holography," Phys. Rev. Lett. **98**, 233901 (2007).

26. M. Zuber, T. Koenig, E. Hamann, A. Cecilia, M. Fiederle, and T. Baumbach, "Characterization of 2x3 timepix assembly with a 500 um thick silicon sensor," J. Instrum. **9**, C05037 (2014).

27. J. L. Starck, F. Murtagh and A. Bijaoui, *Image Processing and Data Analysis, The Multiscale Approach* (Cambridge University, 1998).

---

1. Introduction

The in-line germanium Bragg Magnifier Microscope (BMM) [1] is an imaging system composed of highly asymmetric germanium crystals, geometrically magnifying the X-ray beam in both the horizontal and the vertical direction. The specimen of interest is placed before the BMM and the beam containing the information about the sample is then magnified by means of extreme asymmetric diffraction by dislocation free germanium crystals. X-ray magnification using this concept was initially demonstrated using asymmetric silicon crystals [2–8]. More recently, the use of dislocation-free germanium crystals was demonstrated to be more efficiently due to the larger structure factor of germanium compared to silicon [9]. After the magnification, the X-ray image is detected by a single photon counting semiconductor detector (e.g. Medipix detector was used in [1, 9]). Instead of converting X-ray photons to visible photons and magnifying the visible light image with a diffraction limited microscope and successive detection with a CCD, which is typical in many X-ray imaging schemes, the magnification of the X-ray beam itself and its direct detection provides much higher efficiency [1]. The resulting image of the sample is highly defocused, in practice it is the in-line hologram of the sample image, containing a number of Fresnel fringes. To obtain the sample image one would need to invert the

hologram, i.e. to numerically back-propagate the wavefield onto the sample plane. However, the quantity measured by the detector is the intensity (i.e. the square modulus) of the wavefield, as the phase information is lost and the back-propagation cannot be performed in a trivial way. This is know as the phase problem, the question about existence of the solution of such a problem was firstly raised by Pauli [10], later recognised in crystallography [11] and present in different ways in imaging methods as well. To recover the phase shift just after the sample one can use iterative phase retrieval algorithms [12–14], which iterate the complex wavefield back and forth between sample and detector plane, and apply known constraints on either plane. Another group of phase retrieval algorithms are based on deterministic methods [15, 16] or measuring the intensity of holograms at several positions along the optical axis and successive phase retrieval [17]. Typical applications of iterative phase retrieval use free-space propagation. Therefore for the successful use of iterative phase retrieval algorithms to the BMM holograms, it is absolutely crucial to understand the image formation in such a complicated system. A phase retrieval method considering a BMM composed of two crystals including propagation onto incline planes was already proposed by [18] but the successful phase retrieval was not yet shown.

In general, the BMM is not a linear shift invariant imaging system, which means that its transfer function varies with the position along the plane perpendicular to the optical axis. This is caused by the propagation of the X-ray wavefield onto inclined planes and the successive spatial frequency compression by asymmetric diffraction in the crystals diffraction planes.

In this work, we describe the conditions under which the BMM can be considered a linear shift invariant imaging system. The model is verified by experimental data. Furthermore, we introduce the model for forward image formation with a BMM and compare simulated images with the experimental data. Finally a phase retrieval of experimental holograms of a phantom sample (polystyrene spheres) and a biological sample (spider leg) is performed to show the system image capability.

The paper is organized as follows: in Sec. 2 we describe the conditions under which the BMM acts a linear shift invariant system and compare the model with experimental data. In Sec. 3 we give the theoretical description of the image formation in a BMM and compare the simulated data produced with this method with experimental data taken with synchrotron x-rays. In Sec. 4 we describe the iterative phase retrieval procedure that we devised to retrieve the sample image from the in-line holograms. The procedure is employed to obtain quantitative phase image of polystyrene spheres and a proof-of-concept retrieval of spider leg micrographs. Finally, Sec. 5 contains the conclusions.

2. Bragg magnifier microscope as linear shift invariant system

The BMM consists of four successive asymmetrically cut germanium crystals. The geometry of the setup was reported in [1]. In general, each asymmetric crystal (Bragg Magnifier) is not a linear shift invariant imaging system. Referring to Fig. 1, the asymmetric (non specular) reflection corresponds to the propagation of the wavefield onto an inclined plane. Therefore, when the wavefield emanating from the sample intercepts the crystal surface, the free space propagation distance for points at the sample plane at different positions along x-direction, is different. The consequence is that every such a point along the x-direction experiences a different transfer function and thereby the imaging system is not linear shift invariant (i.e. in practice the sample image would differ if the sample would be rigidly translated along the x-direction). The mathematical modelling of image formation with such system is not trivial and also not very practical. If the system under some circumstances can be considered as linear shift invariant, the transfer function of the points at the sample plane would be the same across the field of view (FOV) at any given propagation distance. Then, the mathematical treatment would

be largely simplified because the standard free space propagators (between planes orthogonal to the optic axis) would be well suited. Clearly, when the propagation distance z in Fig. 1
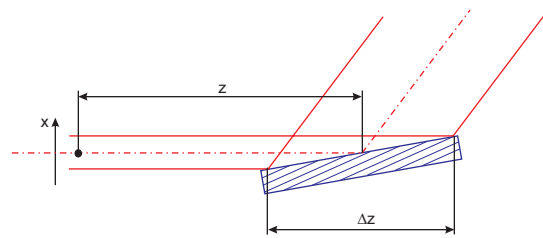

Figure 1. Schematic drawing of the variation of the propagation distance for the points at the sample plane along the x-direction in the case of asymmetric diffraction.

is much larger than the propagation distance difference Δz, the system approximates being a linear shift invariant system for practical cases. To prove this statement a simple experiment was performed. We placed the sample – the edge of a Kapton foil – before the magnifier at opposite sides of the FOV. For each position we recorded images at two propagation distances between the sample and the first Bragg Magnifier crystal. The distances were chosen to be 131 mm (small distance) and 668 mm (large distance) respectively, and the results are shown in Fig. 2.
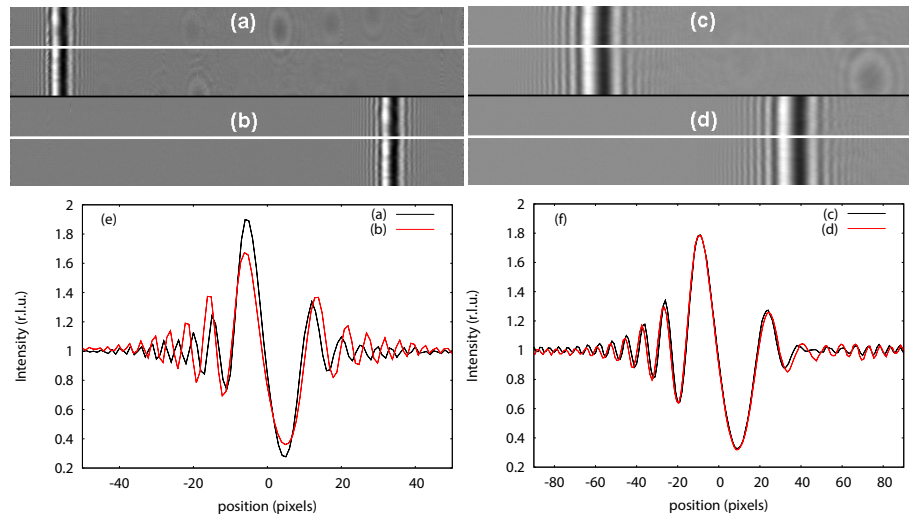

Figure 2. The images of the Kapton edge at the opposite sides of the field of view at propagation distance 131 mm (a)–(b) and at the propagation distance 668 mm (c)–(d). The corresponding 1D profiles (e)–(f).

The in line holograms of the edges are shown in Figs. 2(a) and 2(b) for the small distance and in Figs. 2(c) and 2(d) for the large distance. A line profile, showing the intensity of the Fresnel fringes for each position and each distance are taken. At the small distance, the images of the sample at the right and left side of the FOV are not overlapping and the intensities of main diffraction peak are not the same [Fig. 2 (e)]. For the corresponding profiles when the sample is placed further upstream the Bragg magnifier, we can observe nearly perfectly overlapping

[Fig. 2(f)]. This results is a proof that under some circumstances e.g. if the sample is placed far enough from the BMM, this imaging system can be considered indeed as linear shift invariant.

3. Image formation with Bragg magnifier microscope

If an imaging system is linear shift invariant, then the standard Fresnel propagators (i.e. between the planes perpendicular to the optical axis) can be used to model the forward problem. In this model, the sample is assumed to be illuminated by a plane wave. The sample itself is represented by its transmission function employing the thin object approximation [19]. The wave field just after the sample is expressed as

$$U(x,y) = U_0(x,y)T(x,y), \tag{1}$$

where $U_0(x,y) = \exp\left[2\pi i\left(f_x x + f_y y\right)\right]$ is a plane wave with spatial frequencies f_x, f_y and x, y are the spatial coordinates at the sample plane perpendicular to the propagation direction. $T(x,y)$ is the complex transmission function of the object in this case the projection approximation is used. In order to obtain the wave-field at the detector plane we shall propagate the wavefield $U(x,y)$ through the imaging system which is composed of sections of free space propagation interleaved with crystal complex amplitude functions (later for simplicity referring as crystal functions). The crystal function is in principle the response of the crystal to a given impinging plane wave which can be calculated according to dynamical theory of X-ray diffraction [20]. This can be done in the following way:

1. Calculate the Fourier transform of the wavefield after the sample and propagate it in free space to the position of the first magnifying crystal;

2. Multiply the propagated field by the crystal function;

3. Propagate the resulting field in free space to the position of the second crystal;

4. Multiply the wavefield by the crystal function of the second crystal;

5. Repeat the two steps above for as many crystals as needed, to obtain the wavefield after the last crystal;

6. Propagate the resulting field in free space to the detector position.

This procedure can be expressed mathematically in the following way. A similar approach combining free-space propagation and crystal transfer functions was used before in a more simple type of systems [21–23]. The wave field at the position of the first crystal is

$$\tilde{U}_1(f_x, f_y) = \tilde{U}(f_x, f_y)H_1(f_x, f_y)_{z_1}, \tag{2}$$

where

$$H_1(f_x, f_y)_{z_1} = \exp\left[2\pi i z_1\left(\sqrt{f^2 - f_x^2 - f_z^2}\right)\right] \tag{3}$$

is the free space propagator, z_1 is the distance from the sample plane to the first crystal (central position), f is the frequency and the symbol ˜means Fourier transform. To obtain the wave field after the first crystal we multiply $\tilde{U}_1(f_x, f_y)$ by the crystal function $E_H^1(f_x, f_y)$. The magnification of the crystal is accomplished by rescaling the spatial frequencies by the magnification factor in the direction where such a crystal is diffracting. (in this particular case the horizontal direction, x coordinate). Then the wavefield is propagated to the position of the second crystal

using the free space propagator with transformed frequencies in the horizontal direction. This is written:

$$\tilde{U}_1^c(f_x,f_y) = \tilde{U}_1(f_x,f_y)E_H^1(f_x,f_y), \tag{4}$$

$$\tilde{U}_2(\frac{f_x}{M_1},f_y) = \tilde{U}_1^c(\frac{f_x}{M_1},f_y)H_{1,2}(\frac{f_x}{M_1},f_y) \tag{5}$$

where $\tilde{U}_1^c(f_x,f_y)$ is the propagated field $\tilde{U}_1$ modified by the crystal function $E_H^1(f_x,f_y)$, M_1 is the magnification factor of the first crystal acting in the horizontal direction (x coordinate), $\tilde{U}_2(\frac{f_x}{M_1},f_y)$ is the field with transformed frequencies in x-direction and propagated in free space to the position of the second crystal. To obtain the field at the position of the third crystal we apply the same procedure as above which can be expressed as follows:

$$\tilde{U}_2^c(\frac{f_x}{M_1},f_y) = \tilde{U}_2(\frac{f_x}{M_1},f_y)E_H^2(\frac{f_x}{M_1},f_y), \tag{6}$$

$$\tilde{U}_3(\frac{f_x}{M_1M_2},f_y) = \tilde{U}_2^c(\frac{f_x}{M_1M_2},f_y)H_{2,3}(\frac{f_x}{M_1M_2},f_y), \tag{7}$$

where $\tilde{U}_2^c(\frac{f_x}{M_1},f_y)$ is the wave field modified by the second crystal and $\tilde{U}_3(\frac{f_x}{M_1M_2},f_y)$ is the wavefield propagated to the position of the third crystal with scaled frequencies by magnification of the second crystal M_2 acting in the same direction as the first crystal. We repeat the same procedure for the third and fourth crystal, this time the magnification is applied in the vertical direction (y coordinate) and finally propagate the field after the fourth crystal onto the detector plane. We write for the wave field after the third crystal and the wavefield at the position of the fourth crystal:

$$\tilde{U}_3^c(\frac{f_x}{M_1M_2},f_y) = \tilde{U}_3(\frac{f_x}{M_1M_2},f_y)E_H^3(\frac{f_x}{M_1M_2},f_y), \tag{8}$$

$$\tilde{U}_4(\frac{f_x}{M_1M_2},\frac{f_y}{M_3}) = \tilde{U}_3^c(\frac{f_x}{M_1M_2},\frac{f_y}{M_3})H_{3,4}(\frac{f_x}{M_1M_2},\frac{f_y}{M_3}). \tag{9}$$

The fields after the fourth crystal and at the detector position are respectively:

$$\tilde{U}_4^c(\frac{f_x}{M_1M_2},\frac{f_y}{M_3}) = \tilde{U}_4(\frac{f_x}{M_1M_2},\frac{f_y}{M_3})E_H^4(\frac{f_x}{M_1M_2},\frac{f_y}{M_3}), \tag{10}$$

$$\tilde{U}_D(\frac{f_x}{M_1M_2},\frac{f_y}{M_3M_4}) = \tilde{U}_4^c(\frac{f_x}{M_1M_2},\frac{f_y}{M_3M_4})H_{4,D}(\frac{f_x}{M_1M_2},\frac{f_y}{M_3M_4}), \tag{11}$$

where $H_{4,D}$ is the free space propagator for the segment between the last crystal of the BMM and the detector plane. We can rewrite the forward image formation in a simplified way by dropping the spatial coordinates as the successive multiplications of the free space propagators and the crystal functions (with corresponding spatial frequencies) as follows:

$$\tilde{U}_D = \tilde{U}\,H_1\,E_H^1\,H_{1,2}\,E_H^2\,H_{2,3}\,E_H^3\,H_{3,4}\,E_H^4\,H_{4,D} \tag{12}$$

Finally, the observable intensity I_D at the detector is given by:

$$I_D(x_D,y_D) = |U_D(x_D,y_D)|^2 * \mathrm{PSF}, \tag{13}$$

where $U_D(x_D,y_D)$ is the wavefield in the spatial domain at the detector plane with spatial coordinates x_D and y_D, symbol $*$ is the convolution operator and PSF is the point spread function of the detector.

To test this approach we performed a numerical simulation based on Eq. (12) and compared it with the experiment. The sample used was composed of PMMA spheres with diameter of 20 μm. The used energy was 10.7 keV, the magnification factors of the four BMM crystals were $M_1 = 66.36$, $M_2 = 2.42$, $M_3 = 70.37$ and $M4 = 2.44$ respectively. The crystals were adjusted to the maximum intensity of their rocking curves. This amounts to a total magnification of 160.57 and 171.76 in the horizontal and vertical direction respectively. The simulation parameters were set to the same values as used in experiment. The comparison of simulated and experimental data is shown in Fig. 3. The agreement between the two images is very good.
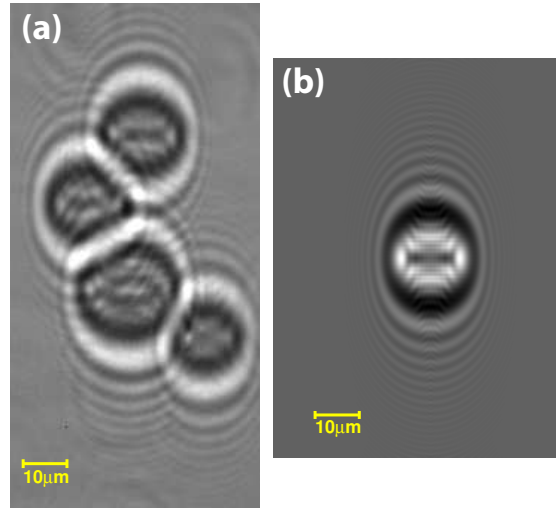

Figure 3. The measured hologram of PMMA spheres at B16 of Diamond light source (a) and the forward image simulation of the single PMMA sphere (b).

Importantly, the asymmetry of the Fresnel diffraction pattern is well reproduced in the simulation. This effect can be simply explained to be caused partially by the different magnification between the horizontal and vertical direction but mainly due to the finite distance between crystals magnifying in horizontal and vertical direction. In case of asymmetric diffraction, the width of the intrinsic rocking is a function of the asymmetry angle. For the extreme asymmetric diffraction the input rocking curve width $\Delta\theta_{in}$ is much larger than the output rocking curve width $\Delta\theta_{out}$, the ratio between the two being the magnification factor for the given crystal:

$$\frac{\Delta\theta_{in}}{\Delta\theta_{out}} = M. \tag{14}$$

As we described in the previous section, the asymmetric diffraction acts as a frequency compressor in the diffraction plane of each crystal, producing rescaled output spatial frequencies in such a plane. This situation for the case of single asymmetric crystal is sketched in the Fig. 4.

The different input and output widths of the rocking curves has a very important consequence for practical image formation. The actual free space propagation distance z before the asymmetric crystal is also rescaled to an effective propagation distance z' behind the asymmetric crystal. From Fig. 4 (left) and Eq. (14) we can express the effective propagation distance z' as

$$z' = z \frac{\tan(\Delta\theta_{in}/2)}{\tan(\Delta\theta_{in}/(2M))}. \tag{15}$$
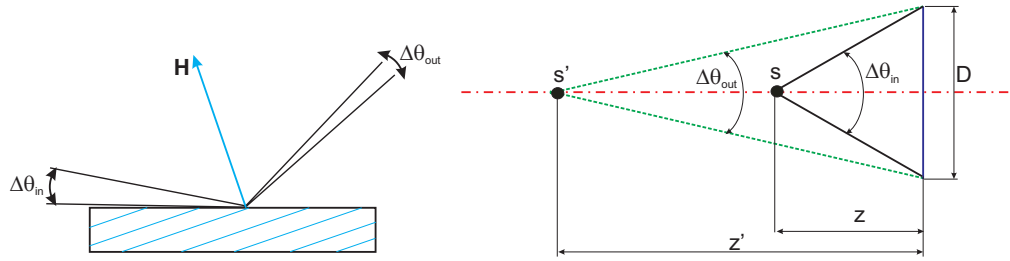
Figure 4. The illustration of spatial frequency transformation by the asymmetric crystal by the transforming the angular input/output widths (left) and the resulting scaling of the propagation distance behind the asymmetric diffraction (right).

Therefore, from Eq. (15), the important consequence can be derived. The wavefield free-space propagates to the first asymmetric crystal then its diffracting and the spatial frequencies are compressed in one direction (in this case in horizontal direction), then the wavefield is propagating again in free space to the position of the next crystal (magnifying again in horizontal direction). In the vertical direction, the wavefield is propagated onto a real distance z but in the horizontal direction (where the frequencies were compressed) the propagation distance is transformed by the Eq. 15 so the corresponding effective propagation distance z' is much smaller in horizontal direction (depending on magnification). This means, that the highly asymmetric crystal is practically "freezing" the free space propagation in the magnification direction while in the perpendicular direction (after diffraction) the wavefield is propagating still onto a real distance. Later the wavefield passes through the vertically magnifying crystals where the same effect occur in the vertical direction. As a result, following our geometry, the recorded holograms at the detector plane are propagated to longer distance in the vertical direction than in the horizontal direction.This is the origin of the Fresnel pattern asymmetry which can be reduced by minimizing the distances between the crystals.

4. Phase retrieval

Phase retrieval from a single detected image is a common problem in coherent diffraction imaging, where iterative error reduction algorithms are used [12].

The phase retrieval procedures in coherent diffraction imaging are performed on the data detected after free space propagation (in far field or Fresnel conditions). However when using the BMM, the near field hologram acquired at the detector encodes the effect of the crystal functions and the relative frequency compressions. Although a unique solution to the phase retrieval for the free-space propagation can be obtained by acquiring data at two different distances [24], this approach makes tomography applications more complicated. Therefore, a number of methods were developed to reconstruct data from a single detected image non-iteratively [16]. This is advantageous both in terms of measurement and data analysis speed. We tested a number of analytical approaches on our BMM data, but with only a limited success. The reconstruction suffered from substantial blurring and thus reduced spatial resolution. There are also many attempts of application of iterative algorithms [12, 25] for phase retrieval from a single image. These iterative methods provided a much higher spatial resolution in case of BMM experimental data. On the other hand, the reconstructed phase maps were typically very unrealistic (see Fig. 5). The algorithm used for reconstruction in this paper is a modification of the one described by Latychevskaia and Fink [25]:

1. Prepare initial guess of the $U(x, y)$, typically array equal to 1.

2. Scale the detected intensity $I_D(x_D, y_D)$ to have intensity equal to 1 anywhere outside the detected object.

3. Propagate $U(x,y)$ from the object plane through the BMM to the detector to get $U_D(x_D, y_D)$.

4. Modify amplitude of $U_D(x_D, y_D)$ to match $\sqrt{I_D(x_D, y_D)}$ of the detected intensity $I_D(x_D, y_D)$.

5. Propagate modified $U_D(x_D, y_D)$ back through the whole system to the object plane to get an updated version of $U(x,y)$.

6. Perform wavelet denoising on $|U(x,y)|$ and $\arg(U(x,y))$.

7. Modify the $U(x,y)$ – wherever $|U(x,y)| > 1$ set $|U(x,y)| = 2 - |U(x,y)|$, while preserve the phase.

8. Go back to step 3.

Wavelet filtering used in this approach is based on [27] and the multi-resolution support: First the image is decomposed based using the A-trous wavelet into several resolutions (typically 3 in our case) and a residual image. This decomposition is essentially described as:

1. Take the image and calculate smoothed image using a low pass filter given for A-trous wavelet (see [27]).

2. Difference of the image and its smoothed version is the first resolution, store for processing.

3. Use the smoothed image as the input in the step 1 to calculate next resolution.

4. The final smoothed image is called the residual image.

All resolutions should have mean equal to 0. At each resolution we define the threshold defining the significant data. Then all pixels within the threshold range are set to 0, thus considering them to be a noise. All other pixels having value outside the threshold are preserved, as they contain significant data. Finally all the resolutions are summed and the residual image to obtain the filtered one.

The thresholds mentioned above can be calculated rigorously based on the noise propagation into different resolutions [27] and the multi-resolution support), but we have used here a more simple approximation. We have simply set the threshold at given resolution to be a $-3 \times \sigma$ and $+3 \times \sigma$, where σ is calculated as a standard deviation of pixel values at given resolution.

The importance of the denoising mentioned above was tested on synthetic data as shown in Fig. 5. We generated the synthetic object composed of three overlapping squares with the phase shifts of 0.2 rad, 0.3 rad and 0.4 rad [Fig. 5(a)] with small absorption. Such object was propagated through the BMM system and the phase was retrieved following the procedure described above with and without wavelet denoising. For the simulation we used photon energy of 10.65 keV and the effective pixel size after magnification 0.31 μm. From the reconstructed data we can see very good agreement of the phase map reconstructed using wavelet filtering [Fig. 5(d)] with the phase of the synthetic object [Fig. 5(a)]. The phase map reconstructed without wavelet filtering suffers from artefacts and the phase values are not corresponding to the original object.

Following the success of the method described above for synthetic data, we applied the method to a number of experimental data. In order to test the method on a well defined sample,
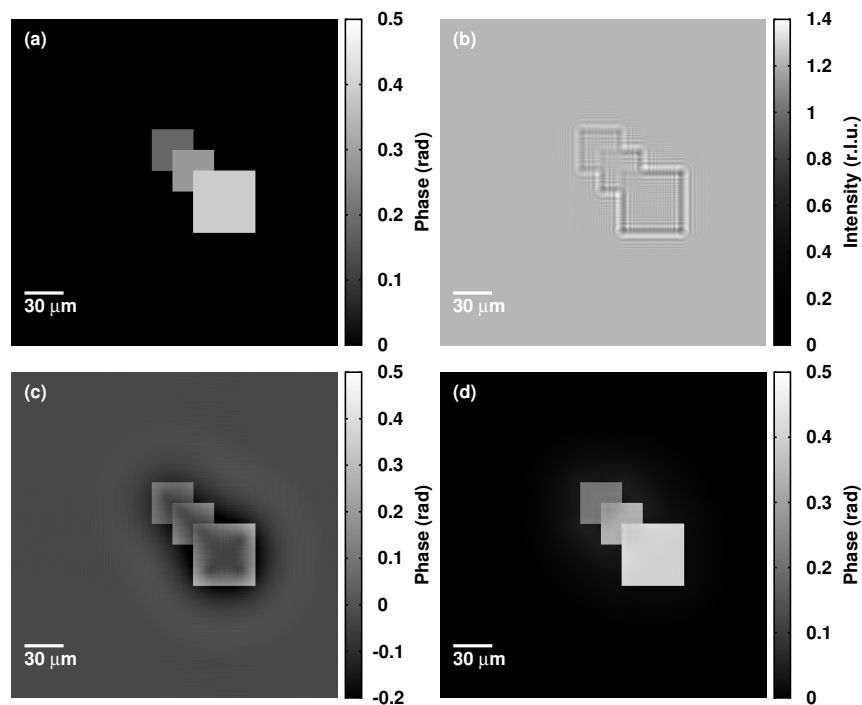
Figure 5. An example of the numerical simulation and its reconstruction by iterative method described in the text. Images represent the phase of the synthetic object (a), detected propagated intensity image after BMM at the detector plane (b), phase map reconstructed without wavelet filtering (c), and the phase map reconstructed with the wavelet filtering (d). Used photon energy was 10.65 keV, propagation distance to the first magnifying crystal was 200 mm, the phase of the squares was set to 0.2 rad., 0.3 rad. and 0.4 rad. Objects were slightly absorbing.

where attenuation can be practically neglected, polystyrene (PS) spheres were used as a test sample. Measured data from Diamond Light Source I13 beamline (Fresnel hologram) of the PS spheres and the successful phase retrieval are shown in Fig. 6. The used photon energy was 10.7 keV, the PS spheres diameter was 10 μm, the magnification at this energy was ˜170-fold and the distance between the sample and the BMM was 720 mm. The countrate at this magnification was 500 counts/s/pixel. The used detector was Medipix Hexa module with 500 μm thick Si sensor material [26]. The phase retrieval was tested for two cases with and without including crystal functions in order to analyse the influence of this on the retrieved phase maps. As it is clear from the line profiles [Fig. 6(c)–(d)], the obtained phase profiles matching very well to the theoretical profile of the PS sphere. The use of crystal functions does not influence much the final result but provides more accurate results. Indeed in extreme asymmetric reflection the blur of the image due to the penetration of X-rays into crystals is very small (smaller by the resolution limit given by the numerical aperture of the system) and does not limit the spatial resolution [9].

The phase retrieval result of the polystyrene spheres hologram is clearly demonstrating the success of the method. To test the robustness of our phase retrieval approach we chose to image a more complex biological object for the phase retrieval reconstruction. An array images of a spider leg was scanned Diamond Light Source I13 beamline. Then images were stitched to
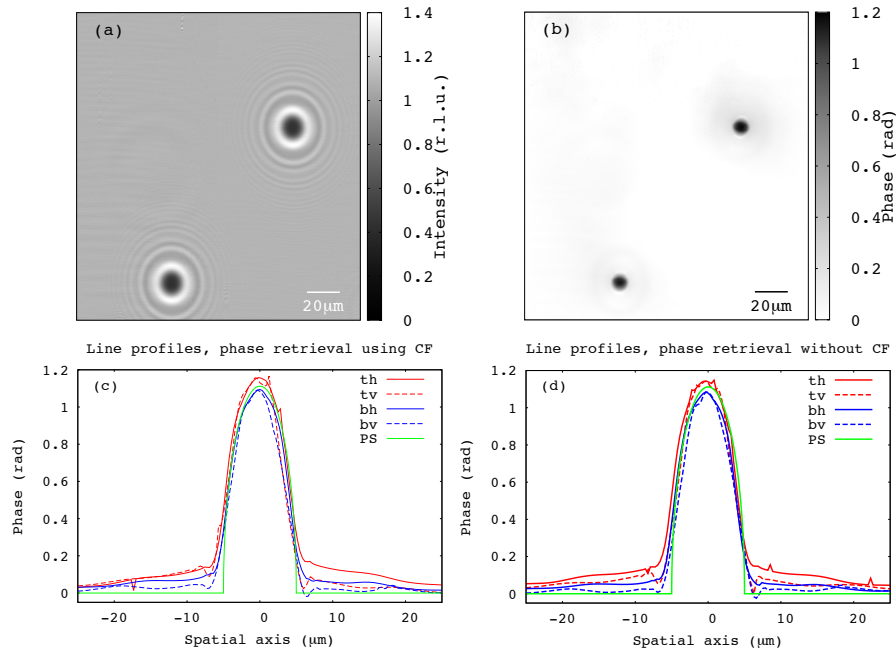
Figure 6. The measured in-line hologram at Diamond Light Source I13 beamline of 10 μm diameter PS spheres (a), retrieved phase map (b), line profiles through the spheres where t,b means top,bottom sphere, h,v means horizontal,vertical profile and PS is the theoretical phase profile through the PS 10 μm diameter sphere. In Fig. (c) for the phase retrieval we used crystal functions (CF) and in Fig. (d) they have not been used. The used photon energy was 10.7 keV and the magnification achieved at this energy was ˜170-fold.

make a single large image and finally the phase was retrieved. The result is shown in Fig. 7. It can be seen that the largely defocused hologram is focused back by our algorithm so the fine structures of the sample are clearly visible. However some parts of the image suffer from phase wrapping which we believed is caused by phase vortexes generated by the sample. Indeed we did not observe vortical structures (or their effect) in case of weak refracting samples, such as the PS spheres and therefore we ascribe them to the sample specific rather than the BMM itself. We will investigate this problem further in future works, to reduce the problem of phase wrapping.
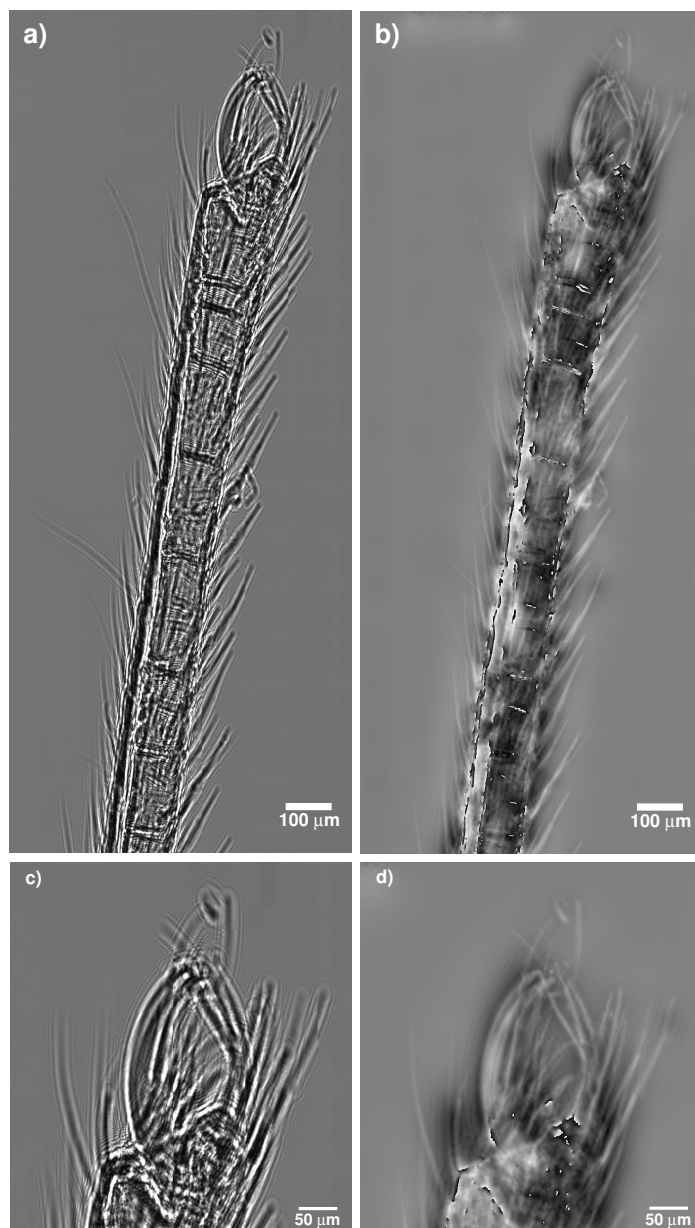
Figure 7. Measured hologram of a spider leg as a result of stitching the number of detected images during a synchrotron experiment (a), retrieved phase map (b) and zoomed areas of the hologram (c) and phase map (d).

5. Conclusion

We developed a single distance phase retrieval technique for the Bragg Magnifier Microscope considering this imaging system to be linear shift invariant. The successful demonstration of this technique is shown on numerical simulation as well as on the measured phantom sample data and biological objects. The obtained phase values are in very good agreement with theoretical values. However, in the case of the biological samples we face the problem of the phase wrapping which in future work we would like to solve. Although images from the experiment at Spring8 BL20XU beamline are not shown here because they contain artefacts due to contaminated crystal surfaces, we reached the count rate of 13375 counts per pixel per second in downstream hutch at the photon energy 10.72 keV. The corresponding magnification was ˜170. This means that acquisition with the time of ˜50ms provides already the images with reasonable signal-to-noise ratio at this beamline. Further optimization in terms of count rate can be achieved and the 1 ms acquisition regime with BMM is possible. This will open up the possibility for quantitative high resolution spatial and temporal imaging of dynamic phenomena e.g. in biological systems with a spatial resolution well below one micrometer.